Full-hemispherical photoelectron-diffraction data from Cu(001): Energy dependence and comparison with single-scattering-cluster simulations

D. Naumović, A. Stuck, T. Greber, J. Osterwalder, and L. Schlapbach
Institut de Physique, Université de Fribourg, 1700 Fribourg, Switzerland
(Received 3 June 1992; revised manuscript received 15 September 1992)

Angular distributions of several photoelectron and Auger transitions have been measured above a Cu(001) single crystal at 16 different kinetic energies between 60 and 1740 eV. The results are presented as 2π full-solid-angle intensity maps—diffractograms—that permit a clear representation of the relative importance of various scattering processes at each energy and the evolution of intensity patterns with energy. The experiments are compared with single-scattering-cluster (SSC) simulations performed at corresponding energies. This serves to probe the accuracy of the SSC formalism over a vast energy and angular range and to illustrate the role of the angular momentum of the final state, polarization effects, and temperature effects. Rather good agreement is found for positions of angular patterns down to very low energies, with problems mainly in relative intensities. The sensitivity of low-energy diffraction patterns to bond lengths is demonstrated.

I. INTRODUCTION

The angular dependence of x-ray excited photoelectron and Auger electron intensities above single-crystal surfaces is by now rather well understood, at least for energies greater than a few hundreds of electron volts.[1,2] Essentially, final-state scattering and diffraction produce intensity maxima along internuclear axes and high-density crystal planes, and more complex intensity modulations elsewhere. Much less is known about how these patterns vary with energy, particularly toward the low-energy end. In this paper we present a very large experimental data set, ranging over almost the full hemisphere above a Cu(001) surface and over kinetic energies from 60 to 1740 eV. This enables us to draw conclusions about the relative importance of several mechanisms contributing to the diffraction at different energies. Some of this has been observed and discussed previously,[1,2] but has not been as clearly evidenced by one complete set of experimental data.

For some selected cases it has been demonstrated that such patterns can be reasonably well described by multiple-scattering[3–5] or even single-scattering (SS) calculations,[1,6–8] and what is really relevant here, that the accuracy of such simulations is high enough to permit a structural analysis of the surface under study. As far as the SS approximation is concerned there are conflicting opinions about its applicability at all, and in particular about the energy range where it can be safely used. On the other hand, its conceptual simplicity and computational efficiency make it particularly appealing for extensive structure searches. It is one purpose of this paper to test the SS model against our extensive data set. All calculations have been performed with a minimum number of adjustable parameters. We chose this particular surface because its structure is well known and because it does not reconstruct.[9]

The development of the calculated intensity patterns with energy is found to parallel that of the experimental data. However, like others[3–5] we encountered particular cases where the SS model fails to well describe the data. The influence of thermal vibrations and of the angular momentum of the final state is also investigated. In the low kinetic-energy diffractograms, a mirror-symmetry breaking due to the oblique photon polarization in our experimental geometry is revealed. Moreover, the sensitivity of such low-energy data to bond lengths is demonstrated. The particular case of the Cu $M_{2,3}$ VV Auger emission is more complex[10] and will be briefly discussed here.

A further motivation for measuring this large set of photoelectron diffraction (PD) and Auger electron diffraction (AED) data over almost 2π solid angle was to verify recently introduced direct Fourier transform methods for obtaining real-space images around the photoemitter.[11,12] The results of such an analysis in terms of photoelectron holography are presented elsewhere.[13,14]

II. EXPERIMENT

The experimental system used was a VG ESCALAB Mark II x-ray photoelectron spectrometer with a base pressure of 3×10^{-11} mbar, with a hemispherical electron energy analyzer and a three-channeltron detector. A two-axis goniometer permits one to perform x-ray photoelectron diffraction (XPD) measurements. A Mg $K\alpha$ ($h\nu=1253.6$ eV) and Si $K\alpha$ ($h\nu=1740.0$ eV) twin anode provides x-ray photons with an incidence direction on the sample that is 54° away from the electron detection direction and $-48°$ out of the plane scanned by the surface normal (Fig. 1).

The spectrometer is interfaced to a dedicated Macintosh II computer, which permits automated recording of two-dimensional intensity maps. The acquisition procedure consists in measuring series of azimuthal (ϕ) scans, during which the crystal is rotated about its surface normal, at polar angle intervals of $\Delta\theta=2°$. It begins at a rather grazing angle of $\theta_{\text{start}}=78°$ of normal and terminates at $\theta=0°$, while the azimuthal step size increases at each polar angle as $\Delta\phi=\Delta\theta\theta_{\text{start}}/\theta$ (Fig. 2). In this

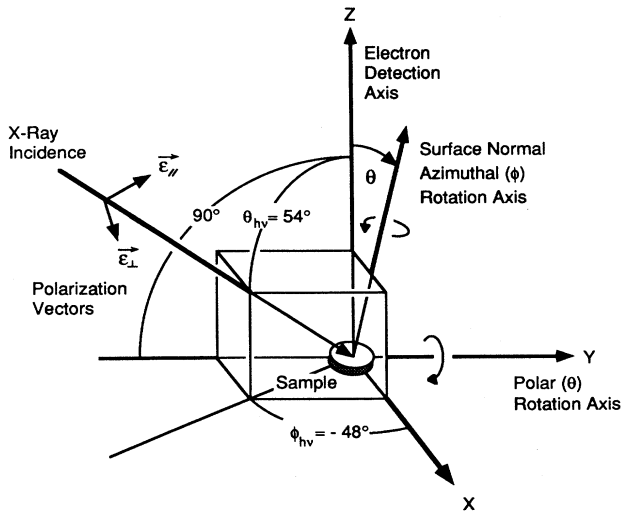

FIG. 1. Schematic representation of our experimental geometry. Incident x rays are described by two orthogonal polarization vectors $\varepsilon_{\parallel}$ and $\varepsilon_{\perp}$; $\varepsilon_{\parallel}$ is parallel to the plane defined by the electron detection axis and the x-ray incidence, while $\varepsilon_{\perp}$ is perpendicular to the same plane. The sample can freely rotate around two axes (polar and azimuthal).

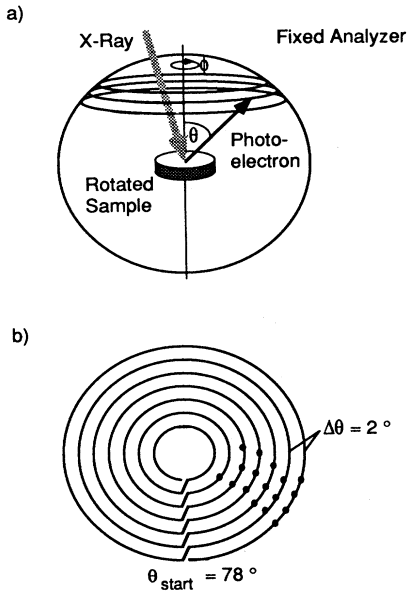

FIG. 2. Diffractogram measuring procedure. (a) The sample is rotated about its surface normal so as to measure an azimuthal scan at each polar angle position. (b) The measurement starts at a grazing angle of $\theta_{start}=78°$ off normal and ends at the normal at $\theta=0°$. The polar angle intervals are a constant $\Delta\theta=2°$ while azimuthal steps increase at each polar angle as $\Delta\phi=\Delta\theta\theta_{start}/\theta$ in order to obtain uniformly distributed angular settings.

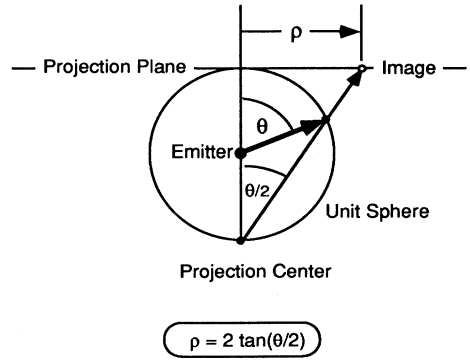

FIG. 3. Stereographic projection.

way about 3600 energy spectra are measured at more or less uniformly distributed angular settings with an angular accuracy of 0.2°. Intensity and background signals are evaluated during acquisition time by a curve-fitting procedure. The two-dimensional data $I(\theta,\phi)$ are visualized in the form of a gray-scale image through a stereographic projection (Fig. 3).

The Cu(001) crystal was prepared using standard techniques.[15,16] Crystallinity of the surface was verified by low-energy electron diffraction (LEED). XPD diffractograms were measured during 8–35 h, depending on the signal intensity, at a pressure of about 5×10^{-11} mbar. Under these conditions the oxygen and sulfur contamination was always maintained below 5% of a monolayer, and below 10% for carbon.

III. SINGLE-SCATTERING-CLUSTER CALCULATIONS

A. Single-scattering-cluster model

For theoretical simulations of photoelectron or Auger electron emission patterns we used basically the same single-scattering-cluster model previously described by Kono *et al.*[6] In order to permit a concise definition of all the input parameters used, we give the SSC formalism in its simplest form, which is that for plane-wave scattering. Here, the intensity of emission from an s initial state (angular momentum $l=0$) into the direction $\hat{\mathbf{k}}$ relative to the crystal is given by

$$I(\mathbf{k})=\left|(\hat{\varepsilon}\cdot\hat{\mathbf{k}})e^{-L_0/2\Lambda_e}+\sum_j(\hat{\varepsilon}\cdot\hat{\mathbf{r}}_j)e^{-L_j/2\Lambda_e}W_j\frac{f_j(\theta_j)}{r_j}\times e^{ikr_j(1-\cos\theta_j)}\right|^2+\text{TDS}\ , \quad (1)$$

where the first term in the coherent summation represents the unscattered wave amplitude and the second term the sum of the amplitudes of the waves which are scattered from the atoms j situated at positions $\mathbf{r}_j$ relative to the emitter. Other quantities appearing in

Eq. (1) are as follows. $\mathbf{k}$ is the photoelectron wave vector, with $\hat{\mathbf{k}}=\mathbf{k}/k$; $\hat{\varepsilon}$ is the photon polarization vector; L_j is the total path length of jth scattering path through the solid; Λ_e is the electron attenuation length; W_j is the Debye-Waller factor describing thermal vibration effects; $f_j(\theta_j)$ is the complex scattering factor at a given scattering angle θ_j; and TDS is the thermal diffuse scattering term.

The proper spherical-wave character of the photoelectron excited from a core level by x rays is considered by using the angular-dependent part of the photoemission matrix element, which in the case of s emission takes the simple form $(\hat{\varepsilon}\cdot\hat{\mathbf{k}})$ for the unscattered wave and $(\hat{\varepsilon}\cdot\hat{\mathbf{r}}_j)$ for the primary wave amplitude at the site of the scattering atom. Spherical-wave effects in the scattering are further accounted for by using a scattering matrix approach described by Rehr and Albers,[17] which has been implemented for XPD by Friedman and Fadley.[18] In this formalism, the complex scattering factor $f_j(\theta_j)$ is replaced by a matrix which in our case has been chosen as 6×6.[17] The scattering of waves with different magnetic sublevels m is treated incoherently, while still retaining interference effects between the $l+1$ and $l-1$ photoemission channels produced by the dipole selection rules. The final wave observed at some point in space is then a superposition of a direct unscattered part and of a singly scattered part, which depends on the positions and the local potentials of the neighbor atoms.

In Auger emission, the selection rules allow more angular momenta into the final state. The relative amplitudes and phases are poorly understood. We use here isotropic spherical waves as source waves, while knowing that this is not rigorously correct, as alignment effects have been predicted and also found experimentally.[19] At high energies (>500 eV), the experimental emission patterns are only weakly dependent on the angular momentum character of the source wave, and we simply treat them as an s wave. At lower energies, we represent isotropic Auger emission by summing incoherently for a given angular momentum l the scattering intensities of the $(2l+1)$ magnetic quantum numbers.[20] The *a priori* choice of l is often problematic, particularly when valence levels are involved in the Auger transition.[10,20,21]

B. Input parameters

We give here a detailed description of the choice of parameters and will discuss the influence of varying some of them later on. The proper choice of the inelastic mean free path Λ_e is and remains a conceptual problem in the single-scattering formalism, where inelastic effects are accounted for by an exponential decay of wave amplitude. Mean-free-path tables and formulas give values for the intensity attenuation. It has been found empirically that SSC theory fits experimental data best if values for Λ_e of half those found in the literature are used.[7,15] The reason for this can be seen in Eq. (1): in the absence of scattered waves, the exponential attenuation factor reduces to the proper intensity attenuation of e^{-L_0/Λ_e} after executing the square of the wave amplitude. The problem with this empirical approach is that the coherence length for wave interference effects is effectively increased by a factor of 2. We therefore used throughout all of our simulations the effective mean free path of $\Lambda_e=\Lambda/2$, where Λ is calculated according to[22]

$$\Lambda[\text{Å}]=\frac{538d}{E_{\text{kin}}^2[\text{eV}]}+0.13(d^3E_{\text{kin}}[\text{eV}])^{1/2}\ , \tag{2}$$

where the interlayer spacing d is in this case $d=a_0/2$ with a_0 the lattice constant of the crystal. One can argue that such a reduction in the effective radius where single-scattering events are important occurs implicitly by correlated vibrations of the lattice.[23] The surface above the top layer, defined as the height up to which inelastic attenuation is effective, was arbitrarily positioned at the Cu hard-sphere radius of 1.276 Å (Ref. 6).

The choice of a suitable cluster size is intimately related to that of the inelastic mean free path. Following the discussion by Osterwalder *et al.*,[7] a cubic cluster of $3\times3\times3$ unit cells was used, with a side length of 10.8 Å. The cluster contains 172 atoms distributed over seven layers. No surface relaxation is included.

The introduction of an inner potential of $V_0=13.5$ eV and of the work function $\phi_0=4.4$ eV (Ref. 24) permits one to consider refraction effects of the photoelectron wave at the surface-potential step. Accordingly, polar positions of diffraction features are slightly shifted away from the surface normal, an effect which is particularly important near grazing emission and at low energies. In conjunction with this shift, a redistribution of intensities in polar direction occurs, because equidistant emission angles inside the crystal are fanned out wider apart near grazing than near normal emission, thinning out the electron flux according to

$$I=I_c\left[\frac{\cos^2\theta}{\dfrac{E_{\text{kin}}^{\text{vacuum}}+V_0}{E_{\text{kin}}^{\text{vacuum}}}-\sin^2\theta}\right]^{1/2}, \tag{3}$$

where I_c is the calculated intensity and $E_{\text{kin}}^{\text{vacuum}}=E_{\text{kin}}-\phi_0$. This contribution to the measured instrumental response function has not been considered previously and goes back to a suggestion by Greber.[25] An additional $1/\cos\theta$ prefactor accounts for the purely geometric increase in measured area with θ.

The partial-wave scattering phase shifts δ_l within the solid have been calculated at each kinetic energy by means of an algorithm, which is based on the muffin-tin potential approximation.[24] The procedure is the same as that used for LEED calculations. The values obtained for δ_l are then entered into the Rehr-Albers formalism in order to calculate the complex scattering matrix. The photoelectron diffractograms have been simulated with the proper angular momentum final states produced in the particular transition, e.g., $l=1$, $m=0$ for s emission or $l=2$ or 0, $m=\pm1$ or 0 for p emission. The relative amplitudes and phases in the cases where more than one emission channel exists are dictated by the photoexcitation radial matrix elements and phase shifts as given by Goldberg, Fadley, and Kono.[26]

Temperature effects are treated in the simple model of

uncorrelated vibrations by introducing Debye-Waller factors W_j as described in Ref. 15. We performed the calculations at an absolute temperature $T=300$ K. The mean-squared displacement of the atoms within the bulk was taken to be 0.0058 Å^2, and at the surface 0.0135 Å^2.

IV. RESULTS AND COMMENTS

A. Experimental data set

The energy spectra in Fig. 4 show all photoelectron and Auger electron signals measured in this study using the twin anode Mg and Si x-ray sources. In Fig. 5 we give an overall summary of our data set from Cu(001). All angular distributions are shown in the stereographic projection (Fig. 3). The center of each plot corresponds to the surface normal and the solid circles outside represent grazing emission along the surface. In Fig. 6 we indicate a few low-index directions and projections of some high-density crystal planes in order to facilitate the discussion. All intensities are represented in a linear gray scale ranging from minimum to maximum intensity in each plot individually, thereby producing the highest possible contrast. The absolute anisotropies $(I_{\max}-I_{\min})/I_{\max}$, which are a convenient measure for the strength of the diffraction effects, are indicated in percent. Note that the two intensity maps shown as Figs. 5(d) and 5(e) have been measured with considerably poorer statistics than the rest. The photoelectron signals here have been excited by a slight oxide contamination ($\sim 3\%$) on our Mg anode, providing a weak signal and a poor signal-to-background ratio. Some of the data presented have been measured previously by other groups[6,15,27–34] and our data are in general agreement with their results.

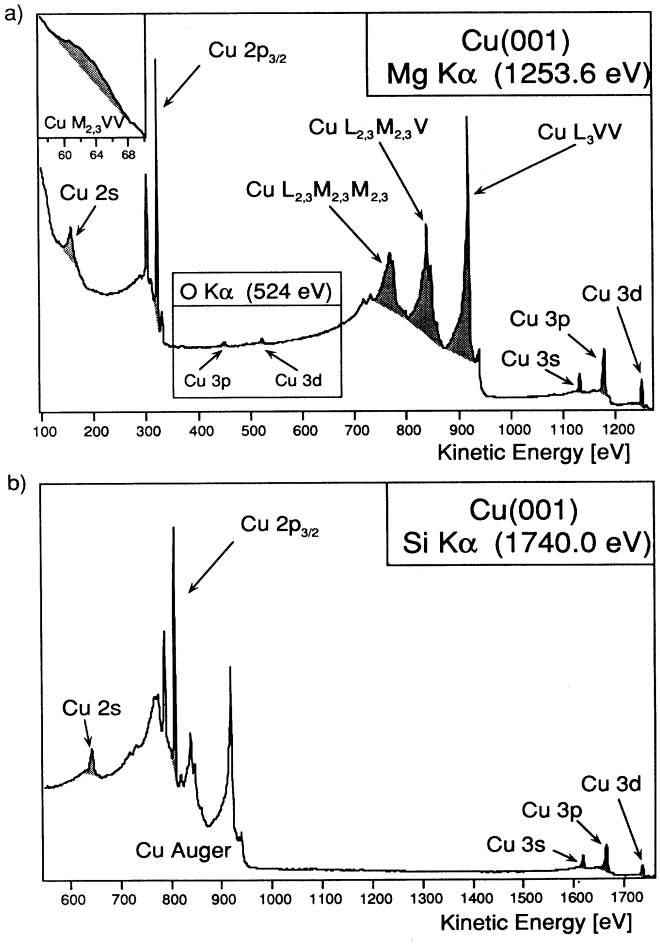

FIG. 4. Overview energy spectra of Cu(001) excited by Mg $K\alpha$ (1253.6 eV) (a) and by Si $K\alpha$ (1740.0 eV) (b) x rays are presented. The energy windows of measured peaks are colored in gray. In the first spectrum (a) the peaks measured with the oxygen contamination of the Mg $K\alpha$ anode (O $K\alpha$ 524.0 eV) are indicated.

The overall symmetry of each diffractogram is due to the lattice symmetry of the crystal, which is in this case face-centered cubic. Notice that the maps are shown as recorded with no symmetry averaging. Comparing all these intensity maps one finds a smooth, continuous development of the patterns with energy, with the only exception of Fig. 5(a), showing the angular distribution of the $M_{2,3}$ VV Auger signal at 60 eV. This is owing to the fact that the wavelength difference is largest between the first two maps, and it is furthermore found that the particular angular momentum character of the source wave is very important for the resulting diffraction patterns at these rather low energies.[10] We shall discuss this latter phenomenon in more detail below.

The evolution of these PD and AED patterns is most easily understood when starting with the highest energies. In Fig. 5(p), Cu 3d emission at 1736.6 eV excited by Si $K\alpha$ radiation is shown. A set of relatively narrow bands of higher intensity dominates this intensity map. According to Fig. 6 these bands coincide with projections of high-density (111)- and (100)-type crystal planes. Similar intensity bands have been observed in photoelectron distributions from Al(001), Pt(110), and Pd(111) at energies above 1000 eV.[31,35,36] They appear thus to be material independent and to be related to Kikuchi bands known from electron microscopy.[37,38] A combination of Bragg scattering off high-density crystal planes and inelastic attenuation produces an intensity enhancement along the projections of these planes, with a width of twice the Bragg angle. At energies between 1 and 2 keV these Bragg angles are typically of the order of a few degrees, explaining the narrowness of the observed bands. Furthermore, many interatomic directions lie naturally along these planes and contribute by forward scattering.

Band crossings coincide with low-index direction. Here, pronounced intensity maxima are found which are associated with the well-known forward focusing of photoelectron flux along nearest- and next-nearest-neighbor bonds ($\langle 011 \rangle$ and [001] directions, respectively).[1,2,39] These features, bands and maxima, can be followed through down to 500 eV, the maxima even down to 150 eV. A systematic broadening of the bands is observed as the energies become lower. This is well explained by the simultaneous widening of the Bragg angles and of the forward scattering with longer photoelectron wavelengths.[1,2] At the same time the intensity modulations along the bands become stronger.

While the bands conserve their shapes and positions over much of the considered energy range, there are other features in the data which show a more pronounced dependence on energy. The evolution of these features is mainly produced by interference effects involving scattering path length differences. Each forward-focusing or zero-order peak along near-neighbor directions has associated with it a first-order constructive interference

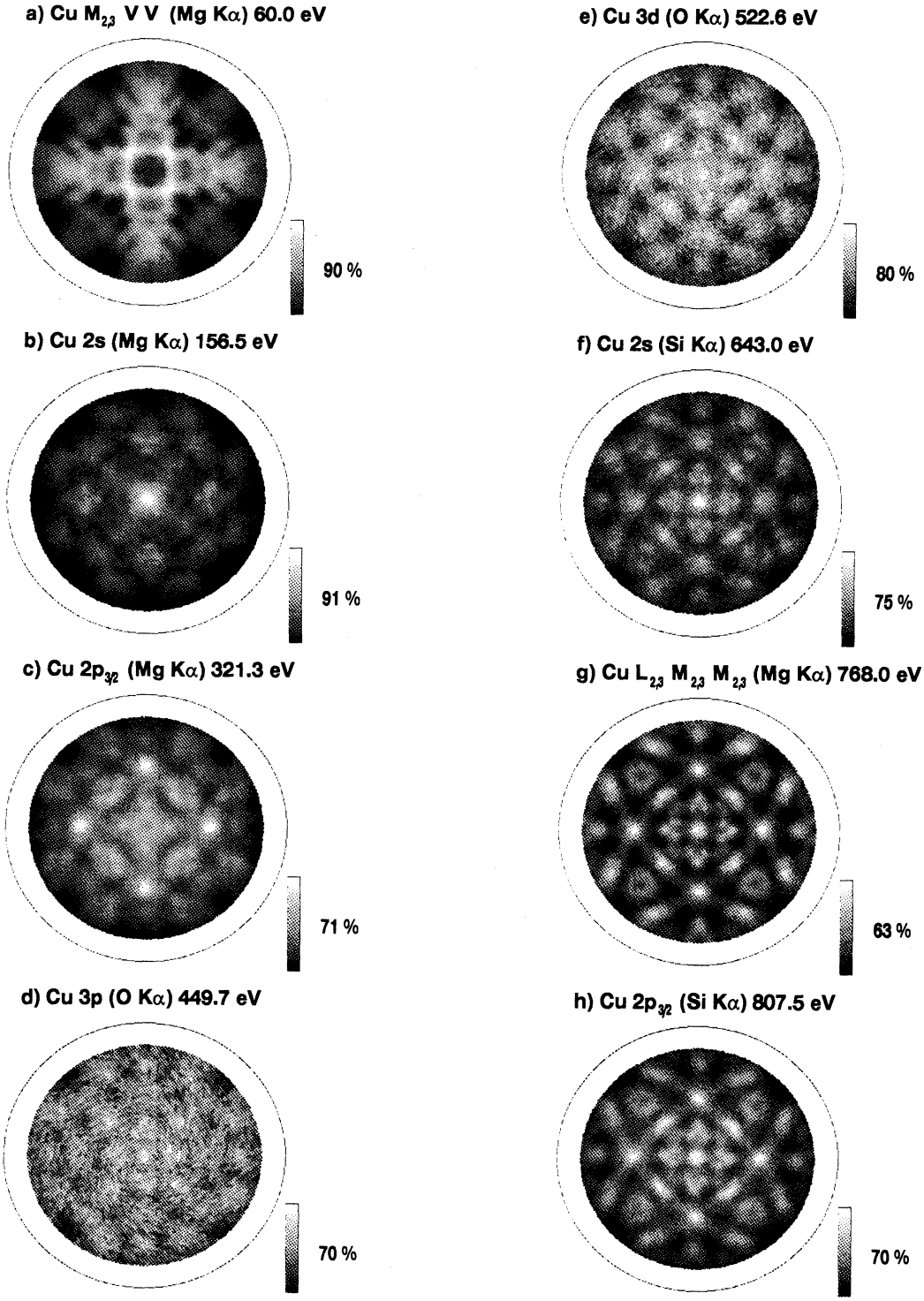

FIG. 5. Experimental data set. The 16 experimental diffractograms (a) to (p) are presented as stereographically projected two-dimensional gray-scale intensity maps. For each diffractogram the measured transition, the excitation source, and the experimental kinetic energy are indicated. On the right-hand side of the gray scale the absolute anisotropy is given as $(I_{\max}-I_{\min})/I_{\max}$ in percent.

cone.[1,2,35] This cone narrows with increasing kinetic energy and thereby creates some alterations in the fine structure. This effect plays a decisive part in the evolution of the eight-leafed flower pattern around the [001] direction, completely enclosed by the {111} Kikuchi bands, of the modulation of intensity along the {111} planes, and of the characteristic patterns along the ⟨111⟩ directions. An additional effect which should also be considered is the appearance of new forward-focusing peaks generated by emitter atoms buried deeper within the surface due to longer inelastic mean free paths at higher energies. In the four following examples [A–D, to

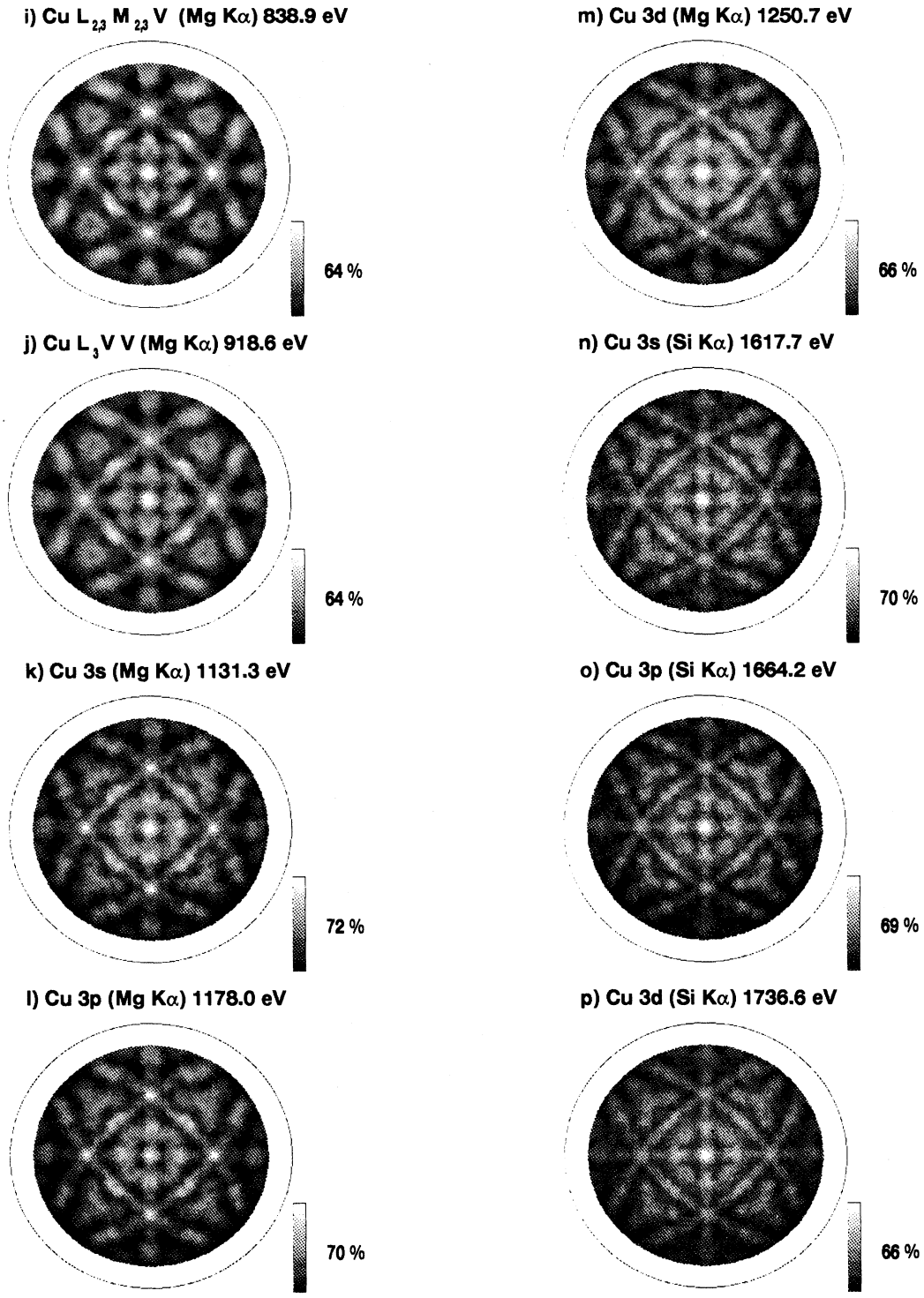

FIG. 5. (*Continued*).

be associated with outlined regions in Fig. 6(a)] we illustrate the interplay between forward-focusing and interference effects. Moreover, we demonstrate that equivalent crystallographic directions are associated with very similar angular patterns: photoelectron and Auger electron diffraction from substrates is predominantly a bulk crystallographic probe if the energy is above 300 eV.

(A) The first-order constructive interferences (see Fig. 12 in Ref. 2), with a phase difference of 2π, i.e., one wavelength, associated with the forward-focusing peaks along [001] and [101] create an intensity enhancement at about $\theta=20°$ in the $\phi=0°$ azimuth and coincide approximately with the [103] forward-focusing peak. In concert these effects produce the first leaf of the eight-leafed flower around the [001] direction. Equivalently, the constructive interferences associated with [101] and [100] (invisible, parallel to the crystal surface) directions create an intensity enhancement at about $\theta=75°$ in the same azimuth and coincide with the [301] direction near the outer rim of the diffractogram. The shape of these ⟨301⟩ features develops quite similar with energy as that of the symmetry-equivalent features much closer to the surface normal.

(B) Interferences of two neighboring ⟨101⟩ directions generate modulations along the {111} planes with maxima, e.g., near [112]. Similar features appear in the [211] direction along the same planes, produced by interferences of the scattering by [101] and invisible [110] neighbors. The narrowing of the associated interference cones with increasing energy can be seen by the appearance of weak minima in the center of the intensity enhancements for energies above 1 keV [Figs. 5(k)–5(p)].

(C) Similar interference phenomena happen between the [001] and ⟨112⟩ directions and create four more petals of the central eight-leafed flower along ⟨114⟩ directions, while on the outer rim of the diffractogram similar interferences appear eight times along ⟨411⟩ directions.

(D) Around the ⟨111⟩ directions we observe ringlike intensity patterns in Fig. 5(f) at 643.0 eV, with minima along ⟨111⟩, which are preserved up to 918.6-eV kinetic energy [Figs. 5(f)–5(j)]. At 1131.3 eV and above they transform into maxima which extend into three branches like a Y [Figs. 5(k)–5(p)]. To understand the evolution of these features, we have to consider the scattering of the photo- or Auger electrons emitted along the cube diagonal of a fcc unit cell (Fig. 7). The electron wave has to penetrate a first triangle formed by the nearest-neighbor face-center atoms and then a second triangle formed by the opposite face-center atoms. Interferences associated with these triangles modify the forward scattering along the ⟨111⟩ directions strongly.[7] Single-scattering considerations have shown that the scattering amplitudes of both triangles are of the same order of magnitude as the forward-scattering amplitude along [111] (see next section).

From considering this large data set we can arrive at

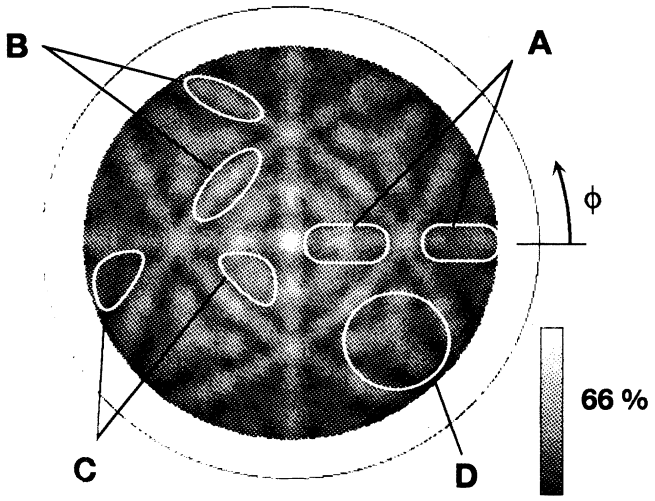

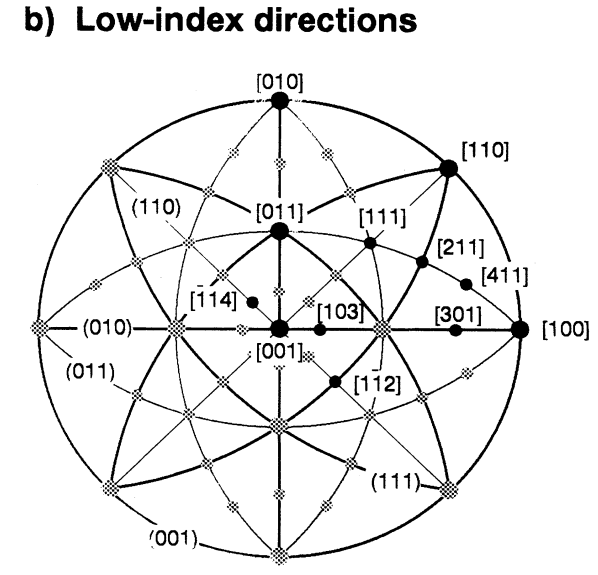

FIG. 6. (a) The experimental angular distribution of Cu 3*d* (Si $K\alpha$) is shown in the stereographic projection. The main interference regions extensively discussed in the text are outlined (A)–(D). (b) The projections of some high-density crystal planes (lines) and the major low-index directions (dots) are drawn in order to facilitate the discussion. The labeled low-index directions are indicated by black dots.

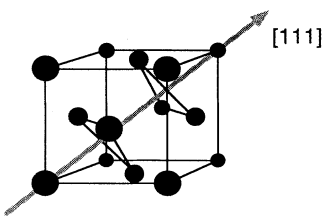

FIG. 7. Emission along the [111] direction in a fcc unit cell. The electron wave has to go through two triangles formed by the near-neighbor face-center atoms before it reaches the opposite corner of the fcc cell to do forward scattering.

some conclusions directly without any further analysis. The final-state scattering at kinetic energies above 500 eV appears to produce patterns that are rather independent of the excitation process, i.e., core or valence photoemission[40] or Auger excitation, although small differences in the overall anisotropies due to the initial states of the electrons can be identified above 768 eV. In this energy range one generally observes lower anisotropies in the

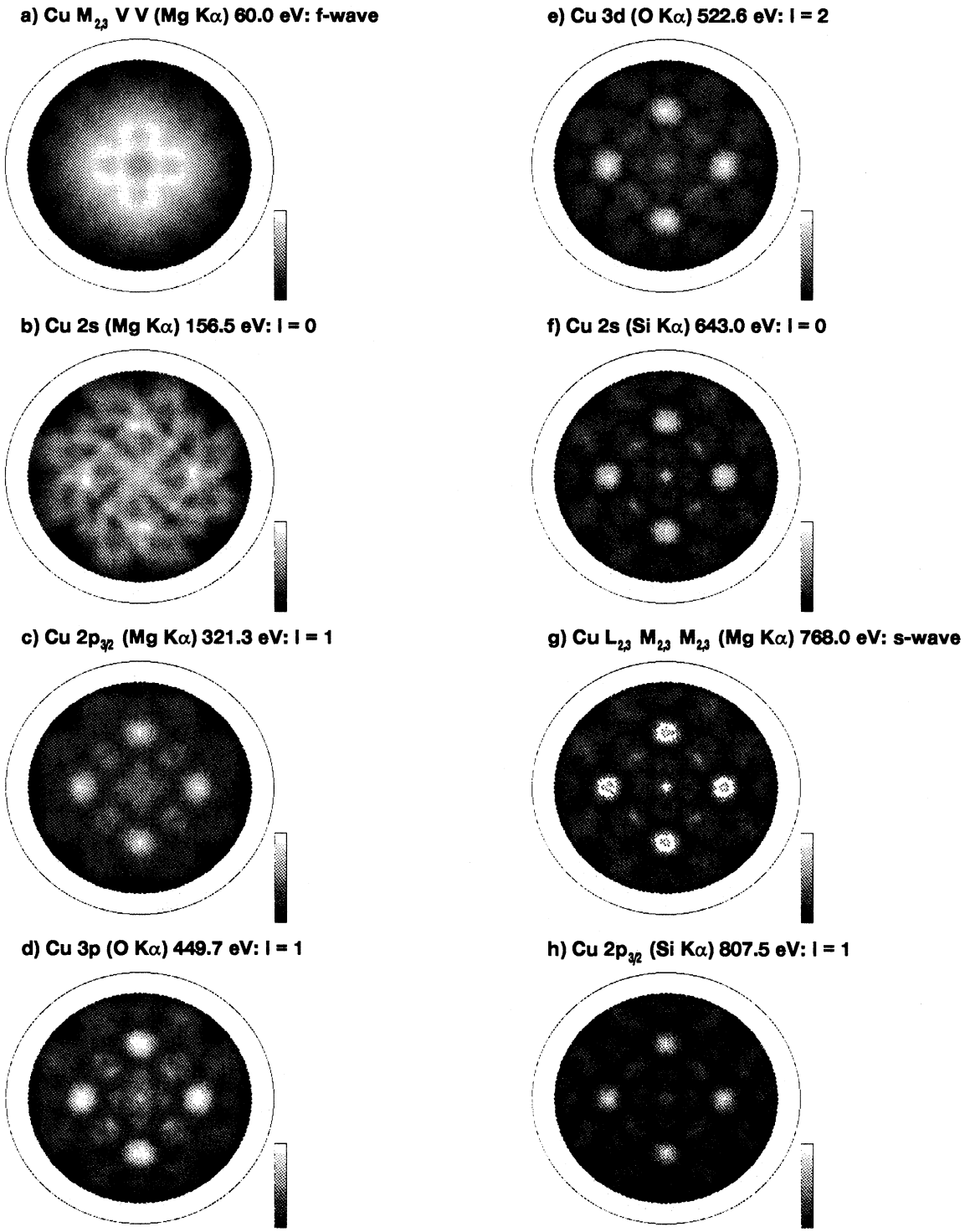

FIG. 8. Simulated data set (SSC). Sixteen calculated diffractograms are displayed in the same way as the experimental ones (Fig. 5). Each transition is characterized by its excitation source, its energy and the initial angular momentum state l for photoelectron emissions or final-state angular momentum for isotropic Auger transitions.

diffraction patterns if the angular momentum of the initial state is high. For example the diffraction patterns of the Cu 3*s* electrons have experimental anisotropies between 70% and 72% [Figs. 5(k) and 5(n)], while the anisotropies of the patterns from Cu 3*d* electrons are about 66% [Figs. 5(m) and 5(p)]. Even lower anisotropies are found for patterns formed by Auger electrons [Figs. 5(g), 5(i), and 5(j)]. As mentioned before, all these patterns are rather insensitive to the surface, and equivalent crystallographic directions exhibit similar patterns independent of

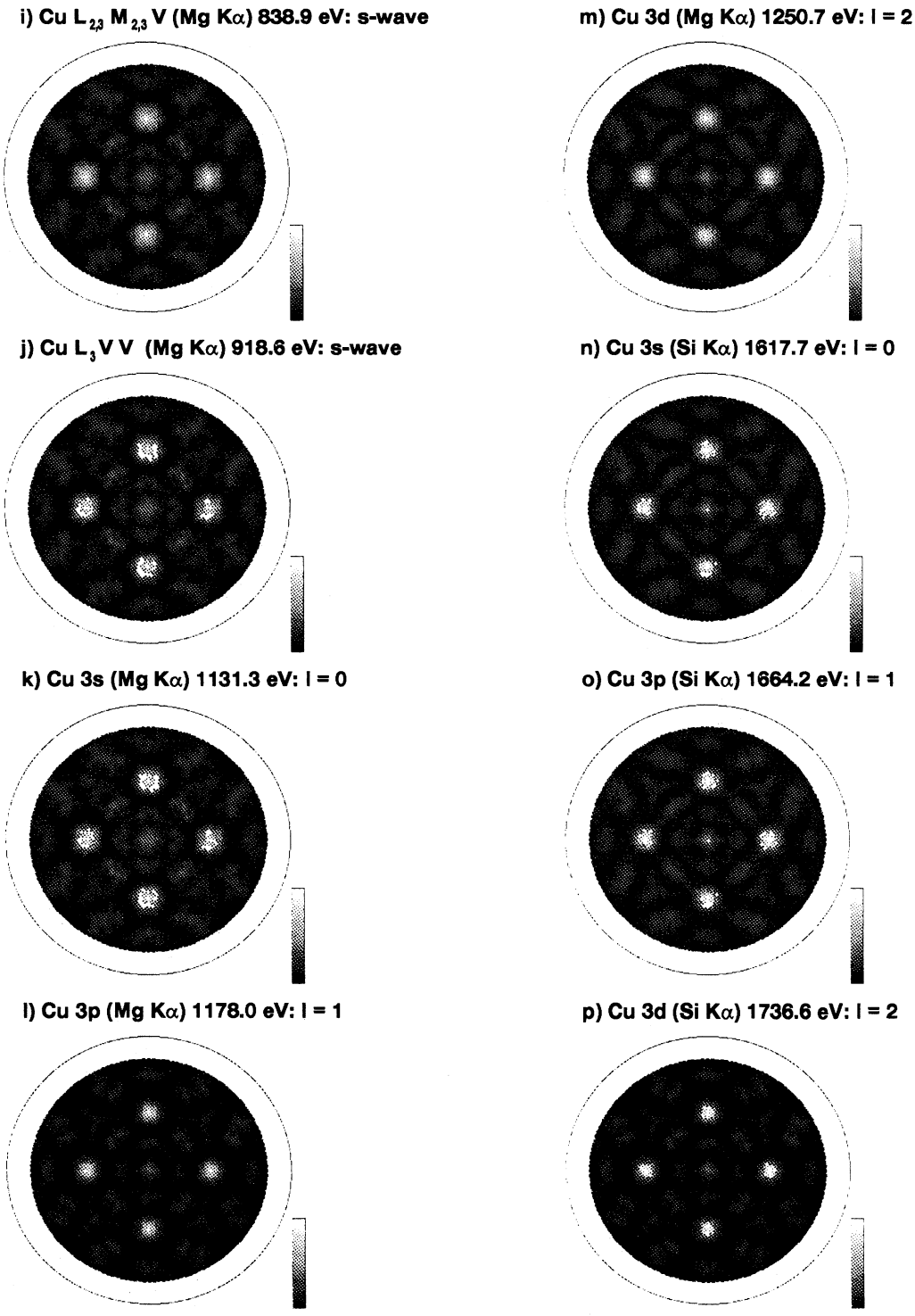

FIG. 8. (*Continued*).

their closeness to the surface. The surface sensitivity is dramatically enhanced at the very low energies, and in particular for the $M_{2,3}VV$ Auger transition at 60 eV, where bulk crystallographic directions can no longer be recognized. Already at 156.5 eV, in Cu 2*s* emission, the [112] direction does not have its replica along [211].

Another phenomenon is visible in Fig. 5(b): a crosslike structure centered at the surface normal is significantly rotated out of the (110) and ($1\bar{1}0$) mirror planes. Our analysis by means of single-scattering calculations (see the next section) reveals that this rotation is due to the oblique photon incidence direction. Likewise, the intensities of four local maxima centered around each ⟨101⟩ direction are such as to break the (100) mirror plane symmetry. We find therefore that photon polarization effects become strong at energies below 200 eV. No mirror symmetry breaking is seen in the 60 eV Auger transition, indicating that this Auger process involves a spherically symmetric source wave.[10]

At the end of this section we want to point out that our diffractograms measured at energies between 500 and 1000 eV are consistent with the Kikuchi patterns at corresponding energies obtained by means of LEED optics (Ref. 29, and also measured at various energies in our laboratory, not shown). This equivalence of PD and AED patterns with Kikuchi patterns has been noticed before.[41,42]

B. Simulated angular distributions

In Fig. 8 we present the full set of single-scattering simulations calculated at energies corresponding to those of our experimental data set (Fig. 5), with input parameters as described earlier. The calculations are shown in the same stereographic projection and in the same linear gray-scale representation as the experimental data set. All diffractograms have been multiplied with an instrumental $1/\cos\theta$ response function and with a refraction factor [Eq. (3)], which makes the simulations fit better to the polar profile of the measured diffractograms. Essentially, this procedure enhances the features at the more grazing polar angles ($\theta > 45°$). Notice finally that the same particular fixed experimental setting is taken for the simulations as has been used in the experiments, i.e., relative positions of manipulator axes, x-ray incidence, and electron detection direction (Fig. 1). However, angular broadening of the x-ray incidence and electron emission has not been taken into account. The angular resolution of the experiments is with 2°–3° high enough to make electron angular broadening effects unimportant on the scale shown in Figs. 5 and 8, and effects due to the angular spread of x-ray incidence directions are weak.[7]

1. High energies (above 1000 eV), effects of the initial-state angular momentum and of temperature

At kinetic energies above 1000 eV [Figs. 8(k)–8(p)], the six simulated photoelectron diffractograms representing 3*s*, 3*p*, and 3*d* emission measured with Mg $K\alpha$ and Si $K\alpha$ radiation are in fair qualitative agreement with the experimental ones [Figs. 5(k)–5(p)], which is consistent with earlier findings for Al(001) and Pt(110) in our groups.[35] All angular features are quite well reproduced in much detail. However, there are some common discrepancies that have been identified as being due to the neglect of multiple scattering:[3,4,43–45] the ⟨101⟩ forward-focusing directions are strongly overemphasized with respect to all other features. For this reason we do not give the absolute anisotropies of the calculated data in Fig. 8, because they would be dominated by these four maxima and could thus not be used for quantitative comparison. The intensity bands along (111)- and (100)-type planes are well reproduced, but they appear much broader in the calculations than in experiment. Including multiple-scattering processes would significantly reduce the role played by forward focusing and would also narrow the intensity bands.[4,45]

In order to give a more quantitative comparison between calculations and measurements, we display two polar cuts at $\phi = 0°$ and 45° (Fig. 9) of the Cu 3*p* diffractogram at 1664.3 eV [Figs. 5(o) and 8(o)], which

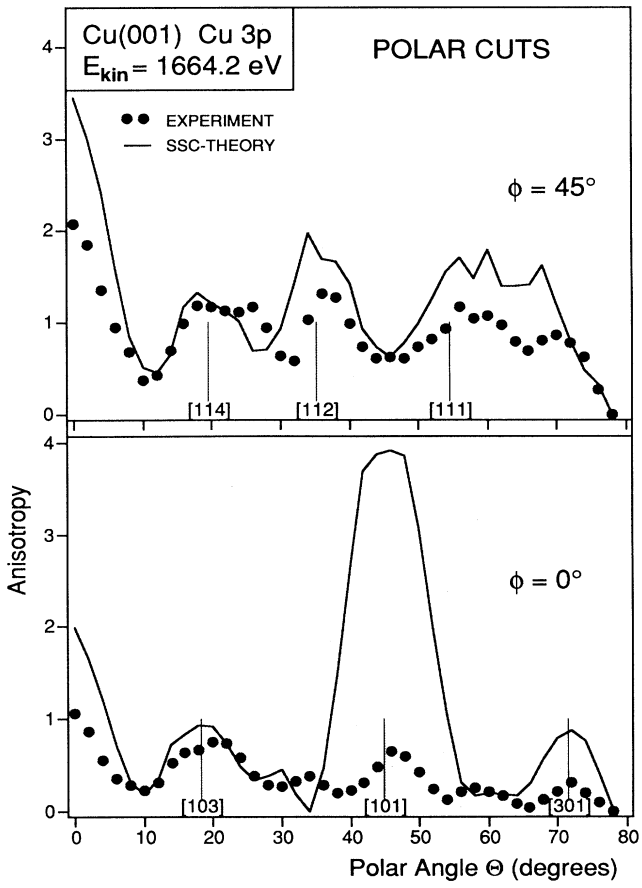

FIG. 9. Polar cuts of the Cu 3*p* diffractogram at $E_{kin} = 1664.2$ eV at two different azimuthal angles $\phi = 0°$ (below) and $\phi = 45°$ (above). The simulated polar profiles (solid line) have been multiplied by an instrumental response and refraction factor [Eq. (3)]. The experimental profiles are represented by black spots. The labeled vertical lines represent the main low-index directions occurring in the mentioned azimuth. We normalized both profiles as $(I - I_{min})/I_{min}$ (see text).

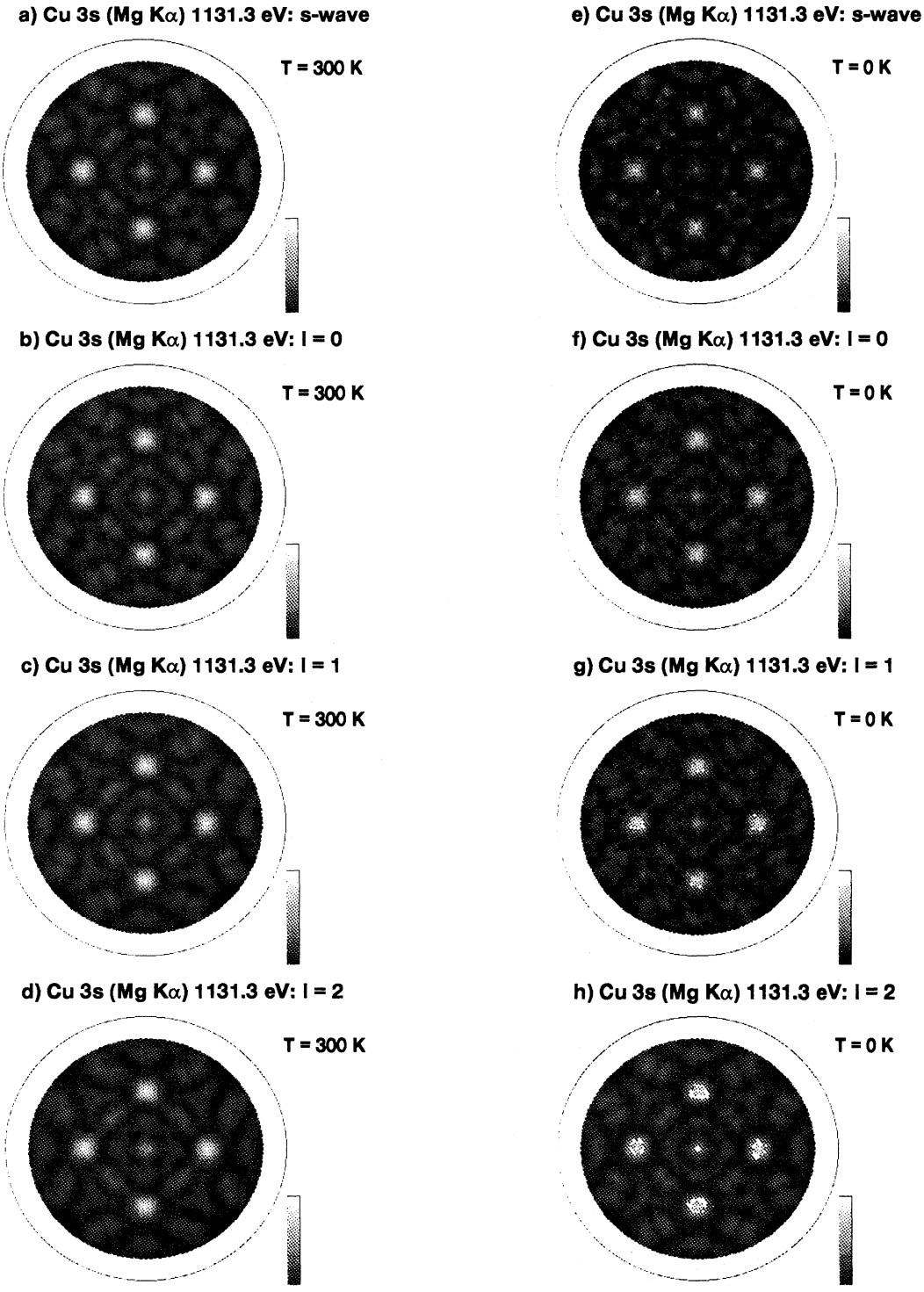

FIG. 10. In order to explore the role of the final-state angular momentum, we present in (a) to (d) four simulated diffractograms at $E_{\text{kin}} = 1131.3$ eV and at a temperature of $T = 300$ K with different final-state angular momenta, i.e., s wave (a), p wave [(b), initial state $l = 0$], $s + d$ wave [(c), $l = 1$], and $p + f$ wave [(d), $l = 2$]. In (e) to (h) we further show diffractograms calculated at the same energy and with identical final states but a fictitious temperature $T = 0$ K, with zero mean-square atomic displacements.

contain the major low-index directions. Because of the known overemphasis of [101] forward focusing in SSC theory, all curves were normalized as $I_{\text{norm}} = (I - I_{\text{min}})/I_{\text{min}}$ rather than normalizing by I_{max} as is otherwise usual. The simulated [101] and to a lesser degree [100] peaks are much broader and more intense than the measured ones, while the maxima appearing in the [103] and [301] directions are reproduced with a much better accuracy (Fig. 9 below). The positions of the peaks are correctly simulated, except for those of the two weaker maxima next to the forward-focusing [101] direction, which are clearly shifted. As discussed in the previous section the $\phi = 0°$ azimuth cuts along the (010) high-density plane, which at this high energy appears quite uniformly intense. The calculated polar profile at $\phi = 45°$ (Fig. 9 above) is in much better accordance with measured anisotropies and positions.

All features that have been previously identified as due to interference effects are very well reproduced. The modulations along the intensity bands, and in particular the splittings due to interferences near ⟨112⟩ and ⟨211⟩ directions described in the next section, are perfectly observable. The more subtle Y-like interference feature along ⟨111⟩ directions can be seen in Figs. 8(k)–8(p), but

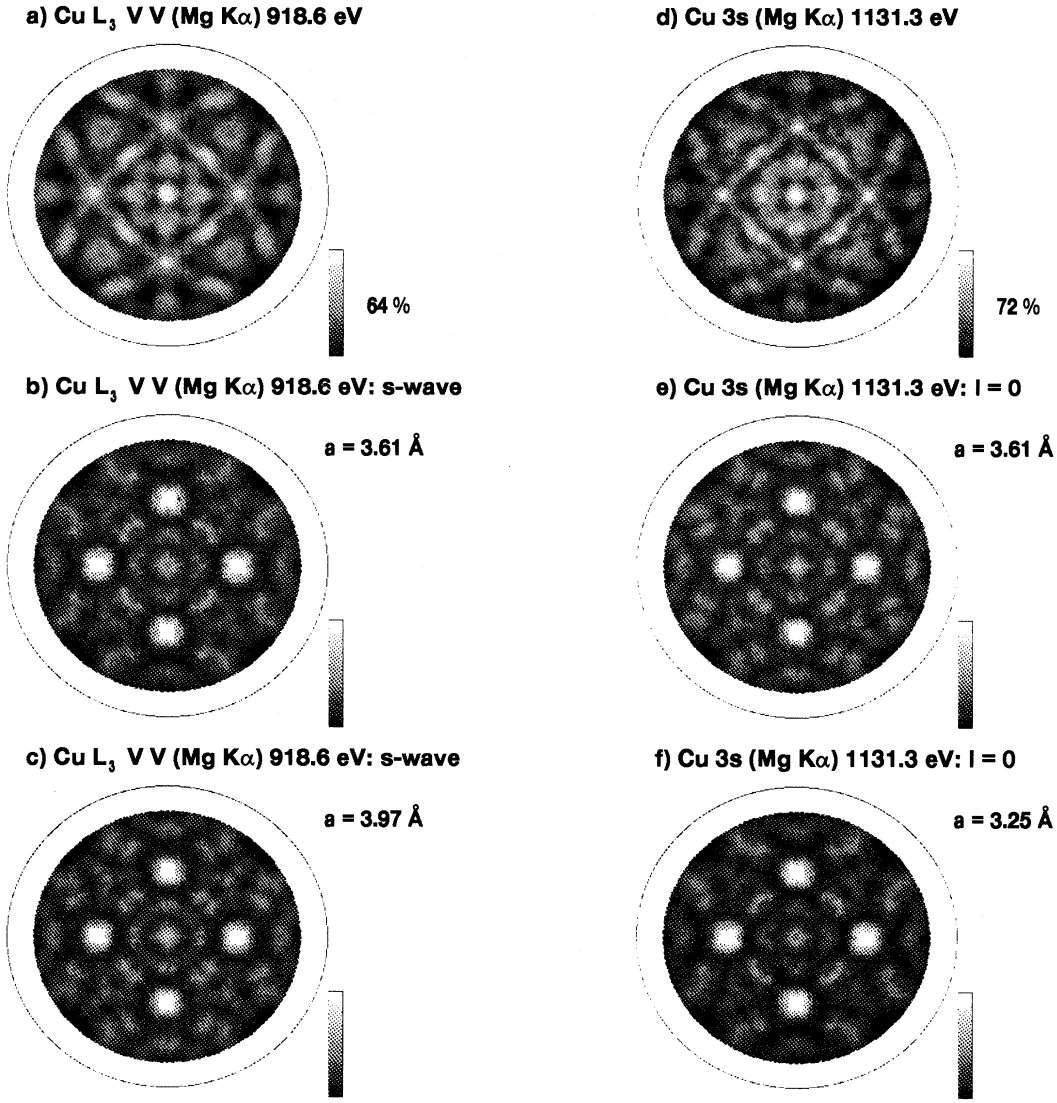

FIG. 11. Interference effects and bond-length sensitivity. In order to check the sensitivity of SSC patterns near 1000 eV to the bond-length variation, we performed simulations with varying lattice constants a. In the experimental patterns, significant transformations occur between the Cu L_3VV (918.6 eV, $\lambda = 0.4$ Å) (a) and Cu $3s$ (1131.3 eV, $\lambda = 0.36$ Å) (d) patterns, which are essentially due to the variation of first-order interference rings. In the four simulated patterns [(b), (c), (e), (f)], we increased the lattice constant of the lower energy simulation from $a = 3.61$ Å (b) to $a = 3.97$ Å (c) and decreased it in the higher energy case from $a = 3.61$ Å (e) to $a = 3.25$ Å (f). In order to emphasize the interference features, the simulated results are displayed with an intensity scale that tops at 60% of I_{max}.

it does not broaden with decreasing kinetic energy as in experiment. The eight-leafed flower patterns centered at [001] and repeated partly around the invisible ⟨100⟩ directions, which also contain interference information (see the next section), are properly simulated in much detail.

At this point we want to discuss two further effects: the role of the initial-state angular momentum and of the temperature. Thanks to the work of Friedman and Fadley,[18] we were able to perform the calculations of Fig. 8 with the proper final-state angular momentum states associated with photoemission from initial *s*, *p*, or *d* states or simply with an isotropic *s* wave. In order to explore these angular momentum effects we calculated angular patterns at 1131.3 eV for the *s* source wave and for *s*, *p*, and *d* emission (*p*, $s+d$, and $p+f$ waves, respectively, with interfering channels for equal magnetic sublevels *m*), which are shown in Figs. 10(a)–10(d), all at 300 K. We then repeated the same calculations at a fictitious temperature of 0 K, i.e., with all mean-square atomic displacements being zero [Figs. 10(e)–10(h)]. At 300 K we observe only a modest widening and smoothing of all features with increasing initial-state angular momentum *l* with no decisive importance for the comparison to experiment at the single-scattering level. At $T=0$ K, however, we find a very pronounced development from a rough, mosaiclike structure for the *s* wave to a smooth structure for higher angular momenta. Presumably, with increasing angular momentum more levels with different phase shifts contribute to the diffraction, washing the pattern out.

The introduction of thermal vibrations by means of a Debye-Waller factor reduces the true interference features relative to the forward-scattering maxima, the latter of which are mostly located along the projection of dense atomic planes. The resulting pattern resembles thus more closely the forward-projected image of the crystal structure and thus the experimentally observed pattern. It is noteworthy that *s* emission seems to be more sensitive to varying temperature than emission from higher angular momentum states. It would be of interest to explore these effects experimentally, especially at lower temperatures by cooling the sample.

2. *Intermediate energies (500–1000 eV)*

In this energy range we present three photoelectron and three Auger electron diffractograms [Figs. 8(e)–8(j)], which continue to be in good agreement with experiment [Figs. 5(e)–5(j)]. The Auger electron diffractograms have here been simulated with an isotropic *s* final-state wave. The overemphasis of the ⟨101⟩ forward-focusing maxima persists. Weak local minima, which are not observed in experiment, appear along the [001] direction in some diffractograms, e.g., in Fig. 8(h), representing Cu $2p_{3/2}$ emission at 807.5 eV, and in Fig. 8(j) for Cu L_3VV Auger emission at 918.6 eV, resulting in volcanolike intensity enhancements that have been discussed earlier.[4] With decreasing kinetic energy, the central eight-leafed flower pattern loses gradually its four ⟨114⟩ directions petals, and the splittings along the (111) intensity bands near the ⟨112⟩ and equivalent ⟨211⟩ directions disappear below a kinetic energy of 918.6 eV, in excellent agreement with experiment. Simultaneously the *Y* patterns centered at the ⟨111⟩ directions change shape and a dip is forming, although we do not clearly observe a ring as in experiment.

As discussed before, these transformations near 1000 eV are mainly due to the constructive or destructive superposition of first-order interference rings associated with different near-neighbor zero-order forward-focusing peaks, and should thus depend on the ratio of the lattice constant and the electron wavelength. The wavelength difference between Cu L_3VV Auger ($E_{kin}=918.6$ eV, $\lambda=0.40$ Å) and Cu $3s$ ($E_{kin}=1131.3$ eV, $\lambda=0.36$ Å) electrons is 10%. In order to explore the sensitivity of these patterns to bond lengths we performed SSC simulations with varying lattice constants while all other parameters remain unchanged. Specifically, we increased the lattice constant by 10% for the lower kinetic-energy simulation (L_3VV) to $a_0=3.97$ Å [Fig. 11(c)] and conversely decreased it by the same amount for the higher energy (Cu $3s$) to $a_0=3.25$ Å [Fig. 11(f)] as compared to the normal copper value of $a_0=3.61$ Å. And indeed, we observe a reversal in the transformation of the discussed features. The splittings near the ⟨112⟩ and ⟨211⟩ directions [out-

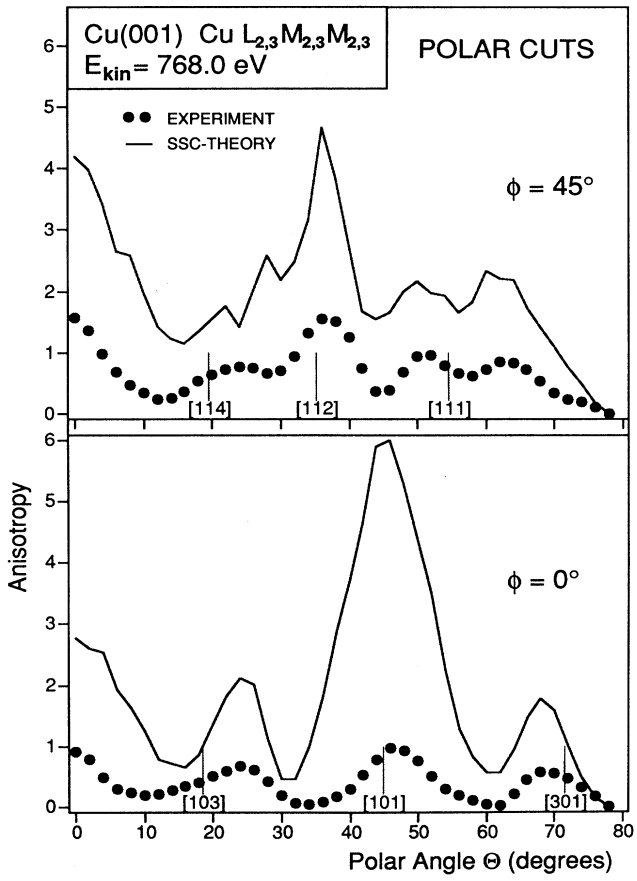

FIG. 12. Same as Fig. 9, but for Cu $L_{2,3}M_{2,3}M_{2,3}$ at $E_{kin}=768.0$ eV.

line B in Fig. 6(a)] appear now in the Cu Auger diffractogram with increased lattice constant while they disappear in the Cu 3*s* simulation with decreased lattice constant. The reversal of transformation of the *Y* pattern into the dip along ⟨111⟩ [outline D in Fig. 6(a)] is more difficult to see. Still, the SSC model is able to describe most of these subtle interference effects correctly, even if it is at the limit of its accuracy.

As for the higher energies we present two polar cuts at $\phi=0°$ and 45° (Fig. 12) of the $L_{2,3}M_{2,3}M_{2,3}$ Auger transition diffractograms [Figs. 5(g) and 8(g)] at 768.0 eV in order to check the quantitative agreement between calculations and experiments. Again the forward-focusing [101] and [100] directions are overemphasized, but the [103] and [301] peaks are also too strong in this case, which may also indicate a problem with the chosen normalization. The positions of all maxima are well reproduced. At $\phi=45°$ the whole profile of the scan agrees very well, but the anisotropy is systematically overemphasized even though the multiplication with the instrumental response and refraction factor [Eq. (3)] reduced this problem considerably.

3. *Low energies (below 500 eV)*

The four lowest energy diffractograms [Figs. 8(a)–8(d)] open the discussion of completely different subjects. We enter here the regime of very short inelastic mean free paths (3–7 Å) and long electron wavelengths (1.6–0.5 Å). On one hand, the electron-scattering amplitudes become more isotropic and much less peaked into the forward direction than at higher energies,[1] which makes multiple scattering seem to be more important. On the other hand, multiple-scattering effects are highly damped due to the very short mean free path of the electrons, which is here of the order of 2–3 atomic distances. The SSC model is naturally not adapted to study these effects, but it proves quite useful to cover a variety of phenomena that become important at these energies: the reduced importance of forward focusing relative to scattering at higher angles, the increasing role played by the final-state angular momentum, and in the same context the appearance of photon polarization effects introduced by nonisotropic electron source wave emission. We should here also be more sensitive to the refraction at the surface potential step [Eq. (3)].

We first discuss the two photoelectron diffractograms representing the Cu $2p_{3/2}$ transition at 321.3 eV [Figs. 5(c) and 8(c)] and the Cu 2*s* transition at 156.5 eV [Figs. 5(b) and 8(b)]. The SSC-simulated diffractogram of Fig. 8(c) reproduces astonishingly well the measured Cu $2p_{3/2}$ pattern at 321.3 eV [Fig. 5(c)]. The diffraction pattern produced at this energy is still vaguely in continuation with the forward-scattering-dominated diffractograms. The nicely simulated cross pattern around the [001] direction replaces the eight-leafed flower pattern. In the simulation [Fig. 8(c)] as well as in experiment [Fig. 5(c)], we observe a weak local intensity dip along the [001] direction (see also Fig. 13), which is probably created by a destructive interference between the forward-focused [001] amplitude and some higher-angle scattering amplitudes emerging in the same direction as discussed by Xu, Barton, and Van Hove.[4] The forward-focusing ⟨101⟩ peaks are still slightly broadened in comparison to experiment. Near the ⟨112⟩ directions the intensity-enhanced feature along the (111) plane is divided into four parts in excellent agreement with experiment. A simulation assuming an *s* initial state and performed at the same energy (not shown) produces more significant differences than at higher energies, as for example an important broadening of the ⟨101⟩ forward-scattering peaks. The temperature effects (not shown) are similar to those at high energies: a roughening of all structures and a narrowing of ⟨101⟩ peaks at 0 K.

The two polar cuts extracted from the Cu $2p_{3/2}$ diffractograms at 321.3 eV [Figs. 5(c) and 8(c)] at $\phi=0°$ and $\phi=45°$ (Fig. 13) show that at these lower energies the overestimation of forward focusing diminishes greatly. The calculated [101] peak is still broader and too strong. As in the previous cases the positions of the maxima are correctly simulated except for a maximum at 30° that disappears into the [101] forward-focusing peak. The profile of the cut in the $\phi=45°$ azimuth and the relative intensities of the maxima are fairly well simulated even if the anisotropy is generally too high in the calculations in spite of the instrumental response and refraction factor

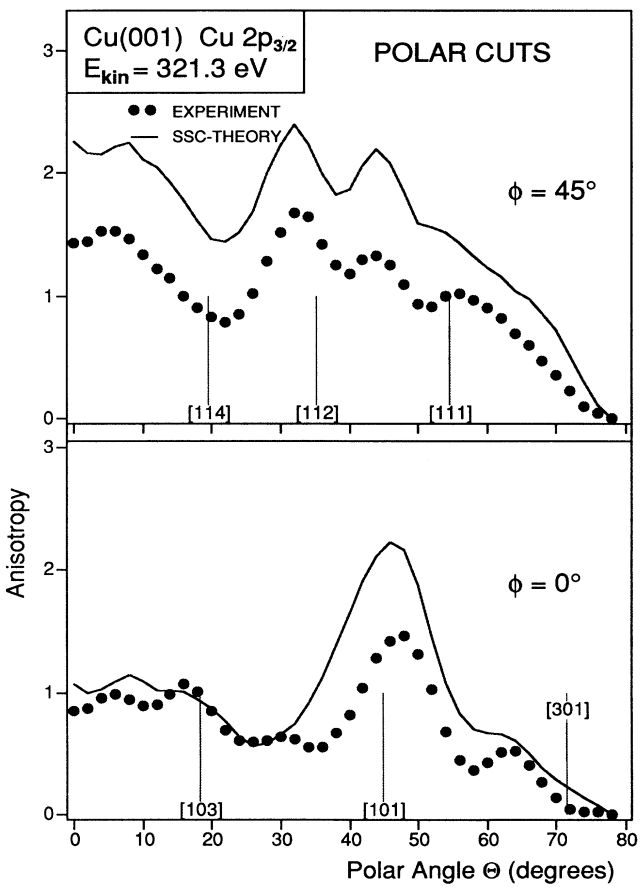

FIG. 13. Same as Fig. 9, but for Cu $2p_{3/2}$ at $E_{kin}=321.3$ eV.

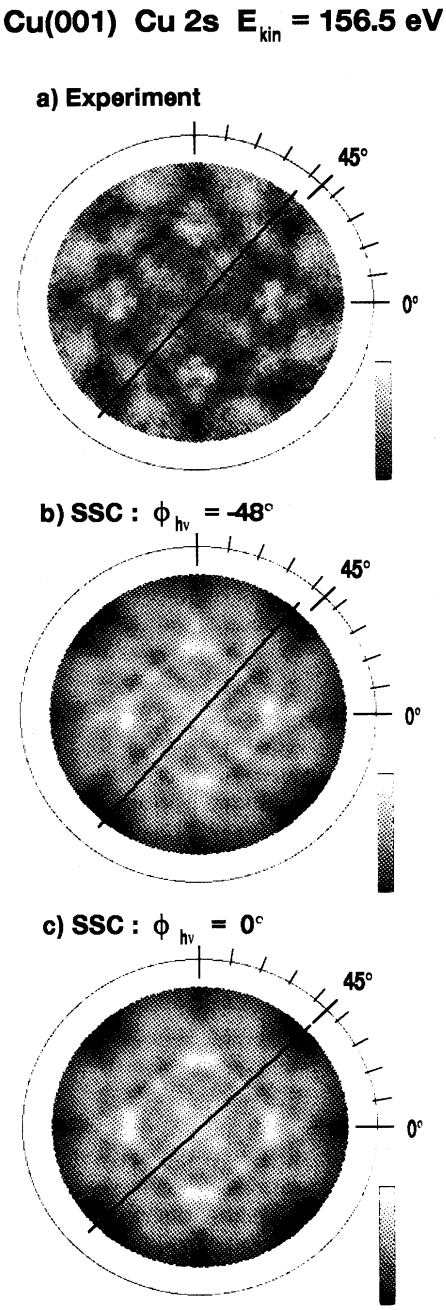

FIG. 14. Polarization effects. The x-ray excitation source being out of the plane defined by the crystal normal and the detection axis ($\phi_{h\nu} = -48°$, see Fig. 1), photon polarization effects appear clearly at low energy as a breaking of the [011] mirror symmetry. In the experimental Cu 2*s* diffractogram at $E_{\rm kin} = 156.6$ eV (a), we observe a significant anticlockwise rotation of about 5° of the central *X* cross with respect to the 45° azimuth. In order to emphasize the observed fine structure, the data here have been normalized at each polar angle by their azimuthally averaged value, which removes all instrumental polar dependence. In (b) we show a SSC simulation with the same geometry as in experiment. In (c) a SSC simulation for the case of a higher-symmetry x-ray source ($\phi_{h\nu} = 0°$) is given.

multiplication [Eq. (3)]. Notice that the minimum which occurs at the normal appears in the simulation as well as in the experiment.

As already discussed before, striking differences in comparison with the higher energy intensity maps appear in the Cu 2*s* diffractogram at 156.5 eV, which is still surprisingly well reproduced by SSC calculations, with one exception: the experiment exhibits an important intensity enhancement along the normal [001] direction, which does not appear as pronounced in the simulation. The characteristic intensity patterns near the ⟨101⟩ directions, with an asymmetric intensity enhancement on their counterclockwise side, appear nicely in the calculation. The central cross pattern shows, as in experiment, an obvious counterclockwise rotation of 5° with respect to the [011] azimuth. In order to clearly illustrate that this asymmetry, which represents a mirror-symmetry breaking for this 4*mm*-symmetry surface, is produced by photon polarization effects, we show in Fig. 14 two simulations for different x-ray incidence geometries: one as

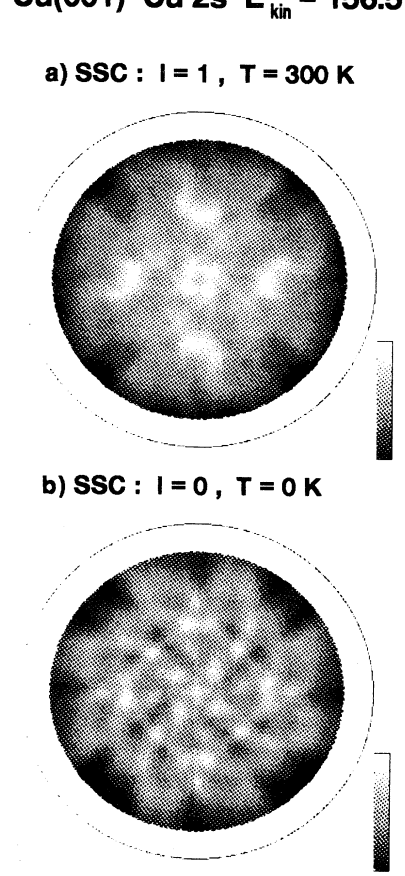

FIG. 15. Initial-state and temperature effects (low energy): A calculated Cu 2*s* diffractogram at $E_{\rm kin} = 156.6$ eV (a), but with an initial-state angular momentum $l = 1$, presents features completely different from the experiment [Fig. 5(b) or 14(a)] and the corresponding $l = 0$ initial-state simulation [Fig. 8(b) or 14(b)]. The $T = 0$ K diffractogram for $l = 0$ (b) does not show significant changes compared to $T = 300$ K [Fig. 8(b) or 14(b)].

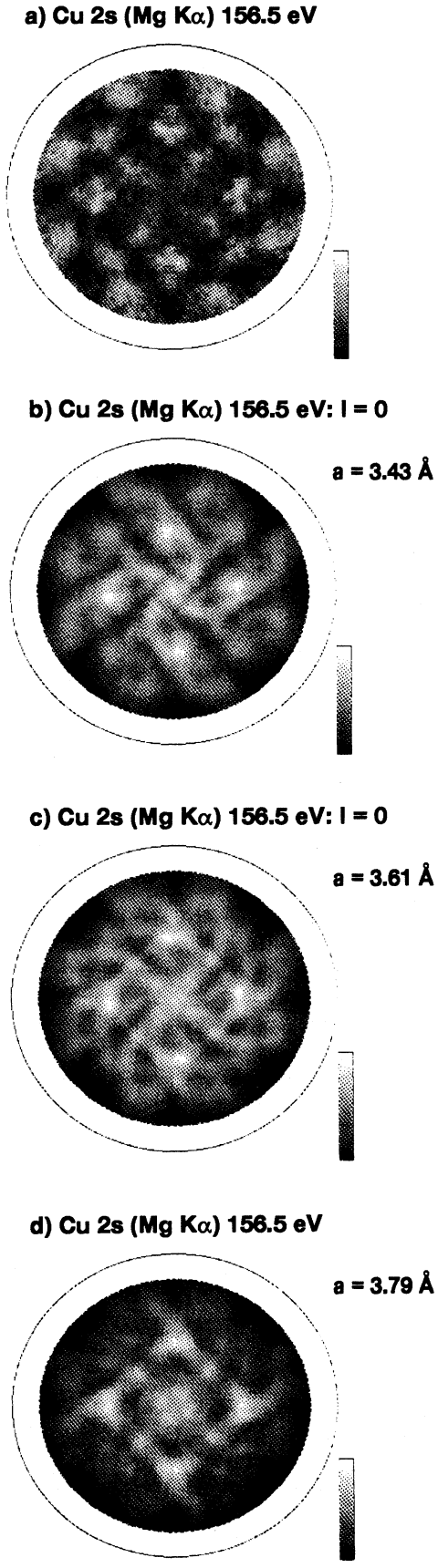

described in Fig. 1, which represents our experimental situation [Fig. 14(b)] and one with the x-ray incidence rotated into the higher-symmetry position defined by $\theta_{h\nu}=54°$ and $\phi_{h\nu}=0°$ [Fig. 14(c)]. Clearly, the experimental diffractogram [Fig. 14(a)] discriminates between the two geometries and favors the experimental setup. In order to study the importance of the initial-state angular momentum we calculated a diffractogram at the same energy but with initial state $l=1$ [Fig. 15(a)], and we obtained a strongly different picture, where, for example, the central cross completely disappeared. The diffractogram calculated for $T=0$ K with $l=0$, on the other hand, does not differ very significantly from the $T=300$ K simulation and essentially shows only a different repartition of relative intensities.

These simulations of photoemission intensities show impressively that the SSC formalism is quite able to model photoelectron diffraction data at such low energies, in contrast to the widespread opinion that a multiple-scattering treatment is mandatory. To corroborate this statement even further, we performed simulations for 2*s* emission from fictitious crystals with varied lattice constants. As shown in Fig. 16 the calculations are very sensitive to a lattice constant modification of 5%. The central cross disappears very fast. We also performed calculations including the known surface relaxation of 2.8%, but we did not observe perceptible changes (not shown).

The angular distribution of the low-energy Cu $M_{2,3}VV$ at 60 eV [Fig. 5(a)] has been the object of several controversial studies in the recent literature.[10,30,34] The theoretical description is in this case complicated, besides the question of the importance of multiple scattering, by two factors: first, the final-state angular momentum composition is not *a priori* known and may be more complex than in photoemission. Our calculation for 2*s* emission at 156.5 eV indicates that a proper treatment of these effects is essential at such low energies, and we present a detailed analysis elsewhere.[10] Second, the transition involves valence levels, and much like in ultraviolet photoemission momentum conservation may lead to additional effects in the angular distributions that are not considered in our local model.

We give in Fig. 8(a) a simulation assuming an isotropic *f* wave, as suggested in Refs. 10 and 20, which is represented by taking the incoherent sum over all magnetic sublevel states m from $m=-3$ to $m=+3$. Clearly, the agreement with experiment is rather poor, and in particular the absolute anisotropy is much lower in the simulation than in experiment. Still, some characteristic features are reproduced, such as the double-cross structure in the center of the image, and the parallel "spines"

FIG. 16. Bond-length sensitivity (low energy): At $E_{\rm kin}=156.6$ eV (Cu 2*s*) a change of ±5% in the lattice constant [(b) and (d)] introduces tremendous changes in the patterns as compared to the experiment (a) and to the simulation with the true lattice constant $a=3.61$ Å (c). In order to emphasize the observed fine structure, the experimental data here have been normalized at each polar angle by their azimuthally averaged value, which removes all instrumental polar dependence.

pointing toward [110]-like azimuths. Simulations using different angular momentum channels completely lack any resemblance.[10] There is definitely a need for developing a more complete theoretical description of such low-energy Auger angular patterns.

V. CONCLUSION

We have presented PD and AED data measured over a Cu(001) single crystal at kinetic energies between 60 and 1740 eV as 2π intensity maps. These substrate emission diffractograms permit to visualize the diffraction pattern in space and their evolution with energy. At energies above 500 eV the patterns represent to first order a forward-projected image of the crystal structure in the surface region. The SSC model, including spherical-wave corrections[17] as implemented by Friedman and Fadley,[18] has been tested against the experimental results with good qualitative agreement for positions of peaks and fine structure. In particular, the interference effects that dominate in the lower energy range are quite well reproduced and permit a rather accurate determination of bond lengths. Nevertheless, we confirm the inherent problem of the SSC model to predict quantitative anisotropies, which is, above 500 eV, essentially due to the overemphasis of forward focusing. For low-energy Auger transitions, it does not take into account all occurring phenomena properly.

As an experimental scheme for a most efficient use of PD and AED effects for studying surface structures we propose a rather quick measurement of diffractograms, possibly at lower angular resolution for a first orientation, and then to perform traditional polar and/or azimuthal scans at higher angular resolution and improved statistical accuracy at carefully selected angles. This method based on the comparison between measured and SSC diffractograms is now being routinely used in our group as a surface probe for further single-crystalline or adsorbate systems where surface reconstruction, epitaxial growth, or surface alloying[36,46,47] are investigated, or for a characterization of angular momentum final states in Auger processes.[10,21]

ACKNOWLEDGMENTS

This work was supported by the Fonds National Suisse pour la Recherche Scientifique. We wish to gratefully thank Dr. M. Shimoda for providing help during experiments, R. Fasel for sharing useful hints during the computer analysis of the results, and Dr. P. Aebi for pertinent and helpful comments during the preparation of the manuscript. We are particularly grateful to Dr. D. J. Friedman and Professor C. S. Fadley for providing their subroutines for simulating spherical-wave effects.

[1]See as review: C. S. Fadley, in *Synchrotron Radiation Research: Advances in Surface Science*, edited by R. Z. Bachrach (Plenum, New York, 1990).

[2]See as review: W. F. Egelhoff, Jr., Crit. Rev. Solid State Mater. Sci. **16**, 213 (1990).

[3]M.-L. Xu and M. A. Van Hove, Surf. Sci. **207**, 215 (1989).

[4]M.-L. Xu, J. J. Barton, and M. A. Van Hove, Phys. Rev. B **39**, 8275 (1989).

[5]A. Kaduwela, G. S. Herman, D. J. Friedman, and C. S. Fadley, Phys. Scr. **22**, 948 (1990).

[6]S. Kono, S. M. Goldberg, N. F. T. Hall, and C. S. Fadley, Phys. Rev. B **22**, 6085 (1980).

[7]J. Osterwalder, A. Stuck, D. J. Friedman, A. Kaduwela, C. S. Fadley, J. Mustre de Leon, and J. J. Rehr, Phys. Scr. **41**, 990 (1990).

[8]J. Osterwalder, T. Greber, S. Hüfner, and L. Schlapbach, Phys. Rev. B **41**, 12 495 (1990).

[9]J. M. MacLaren, J. B. Pendry, P. J. Rous, D. K. Saldin, G. A. Somorjai, M. A. Van Hove, and D. D. Vvedensky, *Surface Crystallographic Information Service, A Handbook of Surface Structures* (Reidel, Dordrecht, 1987).

[10]T. Greber, J. Osterwalder, D. Naumović, A. Stuck, S. Hüfner, and L. Schlapbach, Phys. Rev. Lett. **69**, 1947 (1992).

[11]J. J. Barton, Phys. Rev. Lett. **61**, 1356 (1988).

[12]B. P. Tonner, Z.-L. Han, G. R. Harp, and D. K. Saldin, Phys. Rev. B **43**, 14 423 (1991).

[13]A. Stuck, D. Naumović, H. A. Aebischer, T. Greber, J. Osterwalder, and L. Schlapbach, Surf. Sci. **264**, 380 (1992).

[14]A. Stuck, D. Naumović, T. Greber, J. Osterwalder, and L. Schlapbach, Surf. Sci. **274**, 441 (1992).

[15]R. Trehan and C. S. Fadley, Phys. Rev. B **34**, 6784 (1986).

[16]R. G. Musket, W. McLean, C. A. Colmenares, D. M. Makowiecki, and W. J. Siekhaus, Appl. Surf. Sci. **10**, 143 (1982).

[17]J. J. Rehr and R. C. Albers, Phys. Rev. B **41**, 8139 (1990).

[18]D. J. Friedman and C. S. Fadley, J. Electron Spectrosc. Relat. Phenom. **51**, 689 (1990).

[19]S. Flügge, W. Melhorn, and V. Schmidt, Phys. Rev. Lett. **29**, 7 (1972).

[20]D. Aberdam, R. Baudoing, E. Blanc, and C. Gaubert, Surf. Sci. **71**, 279 (1978).

[21]T. Greber, J. Osterwalder, S. Hüfner, and L. Schlapbach, Phys. Rev. B **45**, 7350 (1992).

[22]M. P. Seah and W. A. Dench, Surf. Interface Anal. **1**, 2 (1979); R. E. Ballard, J. Electron Spectrosc. Relat. Phenom. **25**, 75 (1982).

[23]M. Sagurton, E. L. Bullock, and C. S. Fadley, Surf. Sci. **182**, 287 (1987).

[24]J. B. Pendry, *Low Energy Electron Diffraction* (Academic, London, 1974).

[25]T. Greber (unpublished).

[26]S. M. Goldberg, C. S. Fadley, and S. Kono, J. Electron Spectrosc. Relat. Phenom. **21**, 258 (1981).

[27]L. McDonnell, D. P. Woodruff, and B. W. Holland, Surf. Sci. **51**, 249 (1975).

[28]H. Li and B. P. Tonner, Phys. Rev. B **37**, 3959 (1988).

[29]G. R. Harp, D. K. Saldin, and B. P. Tonner, Phys. Rev. Lett. **65**, 1012 (1990).

[30]D. G. Frank, T. Golden, O. M. R. Chyan, and A. T. Hubbard, J. Vac. Sci. Technol. A **9**, 158 (1991).

[31]Z.-L. Han, S. Hardcastle, G. R. Harp, H. Li, X.-D. Wang, J. Zhang, and B. P. Tonner, Surf. Sci. **258**, 313 (1991).

[32]H. Ascolani, M. M. Guraya, and G. Zampieri, Phys. Rev. B **43**, 5135 (1991).

[33]S. Mróz and B. Stachnik, Surf. Sci. **247**, 201 (1991).
[34]L. J. Terminello and J. J. Barton, Science **251**, 1218 (1991).
[35]J. Osterwalder, T. Greber, A. Stuck, and L. Schlapbach, Phys. Rev. B **44**, 13 746 (1991).
[36]A. Fischer, R. Fasel, J. Osterwalder, A. Krozer, and L. Schlapbach (unpublished).
[37]*Electron Microscopy in Solid State Physics,* edited by H. Bethge and J. Heydenreich (Elsevier, Amsterdam, 1987).
[38]R. Trehan, J. Osterwalder, and C. S. Fadley, J. Electron Spectrosc. Relat. Phenom. **42**, 187 (1987).
[39]H. C. Poon and S. Y. Tong, Phys. Rev. B **30**, 6211 (1984).
[40]J. Osterwalder, T. Greber, S. Hüfner, and L. Schlapbach, Phys. Rev. Lett. **64**, 2683 (1990).
[41]H. Hilferink, E. Lang, and K. Heinz, Surf. Sci. **93**, 398 (1980).
[42]S. Hüfner, J. Osterwalder, T. Greber, and L. Schlapbach, Phys. Rev. B **42**, 7350 (1990).
[43]S. Y. Tong, H. C. Poon, and D. R. Snider, Phys. Rev. B **32**, 2096 (1985).
[44]W. F. Egelhoff, Jr., Phys. Rev. Lett. **59**, 559 (1987).
[45]H. A. Aebischer, T. Greber, J. Osterwalder, A. P. Kaduwela, D. J. Friedman, G. S. Herman, and C. S. Fadley, Surf. Sci. **239**, 261 (1990).
[46]D. Naumović, A. Stuck, T. Greber, J. Osterwalder, and L. Schlapbach, Surf. Sci. **269/270**, 719 (1992); **277**, 235 (1992) (erratum); D. Naumović, J. Osterwalder, A. Stuck, P. Aebi, and L. Schlapbach, *ibid.* (to be published).
[47]R. Belkhou, N. T. Barrett, C. Guillot, A. Barbier, J. Eugène, B. Carrière, D. Naumović, and J. Osterwalder, Appl. Surf. Sci. (to be published); D. Naumović, N. T. Barrett, J. Osterwalder, C. Guillot, and R. Belkhou (unpublished).